

# Molecular dynamics simulation of the effects of neutron irradiation on Caesium Lead Bromide

Zhongming Zhang<sup>1</sup>, Samuel Murphy<sup>1</sup>, and Michael Aspinall<sup>1</sup>

<sup>1</sup>School of Engineering, Lancaster University, Lancaster, LA1 4YW, UK

Corresponding author:  
Zhongming Zhang<sup>1</sup>

Email address: zhongming.zhang@lancaster.ac.uk

## ABSTRACT

With the development of fast neutron reactors and nuclear fusion reactors, it is necessary to find new radiation-hardened high-flux core neutron detectors. The use of perovskite Caesium Lead Bromide ( $\text{CsPbBr}_3$ ) for neutron radiation detection is a new research direction. However, at high temperatures, the effects of neutron radiation, especially the Primary Knock-out Atom (PKA) and Displacement Per Atom (DPA), and the defect distribution at the molecular level have not been reported. This study investigated the effect on  $\text{CsPbBr}_3$  produced by 14 MeV neutron irradiation under 100 K to 400 K. Molecular dynamics methods are used to model the distribution of vacancies and interstitial atoms at the molecular level of materials. This study obtained the displacement threshold energies of three atoms in  $\text{CsPbBr}_3$  and obtained the distribution of vacancies and interstitial atoms within the material over time. Monte Carlo simulations were used to obtain PKA and DPA information in  $\text{CsPbBr}_3$  under neutron irradiation. This research will help to further study the performance changes of halide perovskites under neutron irradiation to verify the possibility of using them as radiation-hardened neutron detectors.

Keywords: Neutron detection; Caesium Lade Bromide; LAMMPS; Geant4; Monte Carlo simulation; Molecular dynamics simulation

## INTRODUCTION

Finding new low-carbon emission energy sources to replace old fossil energy sources is significant for carbon neutrality tasks. Nuclear fusion technology is one of the potential technical solutions. Fusion employs a deuterium–tritium reaction which releases a total of 17.6 MeV of energy almost entirely as kinetic energy, with approximately 14.1 MeV carried by the neutron and 3.5 MeV by the alpha particle. This kinetic energy is subsequently absorbed by the reactor’s breeding blanket, typically composed of lithium-based materials, and converted into heat, which is then used to generate electricity. Its reaction energy release efficiency is extremely high and there will almost be no pollution and nuclear waste [1]. However, the deuterium–tritium reaction releases neutrons with an energy of 14 MeV [2]. According to experience, neutron irradiation with high-energy neutrons causes material embrittlement [3], bringing greater challenges to neutron detectors for fusion reactors. It is essential to develop new neutron detection materials.

$\text{CsPbBr}_3$  is one of the halide perovskites. It has a high average atomic number (Cs: 55, Pb: 82, Br: 35), high resistivity [4], wide bandgap [5], good charge carrier mobility [6] and other advantages; it is a potential candidate for room temperature semiconductor nuclear radiation detection.  $\text{CsPbBr}_3$  has been used to detect gamma, x-ray, etc[7, 8]. In 2021, it was first used for neutron detection with a converter layer [9]. When neutrons collide elastically with an atom, if the kinetic energy imparted by the neutrons is greater than the threshold displacement energy of the lattice site, the atom will be knocked out of the lattice, creating a vacancy and an interstitial atom. Therefore, the threshold displacement energy of a material is an indicator of radiation resistance. However, currently there is little understood about displacement damage in  $\text{CsPbBr}_3$  at different temperatures.

Molecular dynamics simulations evolve a system of atoms in time according to Newton’s second law [10]. It has been successfully used in many simulations of neutron irradiation damage and calculation of threshold displacement energies [11, 12, 13]. Monte Carlo method is a numerical simulation method that takes probability phenomena as the research object. It is a calculation method for estimating unknown

characteristic quantities by obtaining statistical values according to the sampling survey method. Monte Carlo is a famous casino in Monaco. The name of the method indicates the nature of its random sampling. Therefore, it is suitable for computational simulation experiments of discrete systems. In the computational simulation, the random characteristics of the system can be simulated by constructing a probabilistic model that owns the system's similar performance and conducting random experiments on a digital computer [14, 15].

In this study, molecular dynamics simulations were used to predict the threshold displacement energy of three atoms and the radiation damage caused by PKA (34 keV) to CsPbBr<sub>3</sub> crystals. The Monte Carlo method was used to obtain the reactions of high-energy neutrons (14 MeV) with CsPbBr<sub>3</sub>, the PKA energy spectrum and the effect of temperature on DPA.

## METHODOLOGY

### Crystallography and potential

Figure 1 illustrates the CsPbBr<sub>3</sub> structure employed in our molecular dynamics simulations, which crystallises in a cubic lattice. Its space group corresponds to Pm $\bar{3}$ m (No. 221) in the Hermann–Mauguin notation, and the Hall symbol is given as  $-P\ 4\ 2\ 3$ . Lattice parameters have been reported as  $a=b=c=6.017\text{ \AA}$  and  $\alpha=\beta=\gamma=90^\circ$  [16].

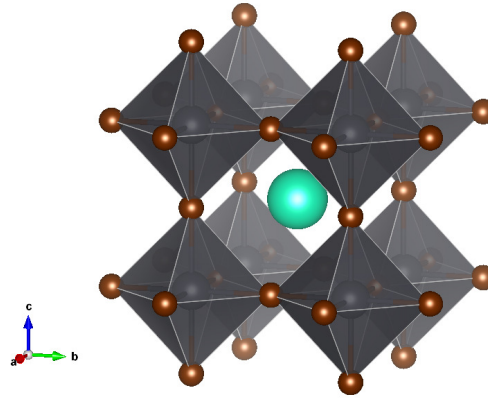


**Figure 1.** Crystal structure of CsPbBr<sub>3</sub> for molecular dynamics simulations.

Molecular dynamics use potential to calculate the atom-atom interaction. The potential model has a significant effect on the result of molecular dynamics simulation. The potentials used in this research are Lennard-Jones 12-6 potential and Coulomb potential. The general form of this potential model is shown in eqs. (1) to (3).

$$V_{LJ}(r_{ij}) = 4\epsilon \left( \frac{\sigma^{12}}{r_{ij}^{12}} - \frac{\sigma^6}{r_{ij}^6} \right) \quad (1)$$

$$V_{coul}(r_{ij}) = 4\epsilon \left( \frac{q_i q_j}{4\pi\epsilon_0 r_{ij}} \right) \quad (2)$$

$$V(r_{ij}) = V_{LJ} + V_{coul} \quad (3)$$

In eqs. (1) to (3),  $i$  and  $j$  are atom labels.  $r_{ij}$  is the distance between two atoms. Specifically, in eq. (1),  $\epsilon$  defines the depth of the potential well, and  $\sigma$  is the separation at which  $V(r_{ij})$  is zero. In eq. (2),  $Q_i$  and  $Q_j$  represent the charges on the two ions.  $\epsilon$  is the vacuum permittivity. It is shown in eq. (3) that the overall interaction is described as a combination of the Lennard-Jones (LJ) 12-6 potential (eq. (1)) and the Coulomb potential (eq. (2)). This potential model was calculated and fitted by Density functional theory (DFT) and was successfully used to predict the phase transfer of CsPbBr<sub>3</sub> [17]. The parameters of the potential model are illustrated in 1.

Furthermore, the Ziegler-Biersack-Littmark (ZBL) [18], illustrated in eq. (4), is splined onto the LJ and Coulomb potential in the cascade simulation at short separations due to it offers a better description of

	$\epsilon(\text{eV})$	$\sigma(\text{\AA})$	$q(e)$
Cs	0.5784	2.927	0.86
Pb	0.01071	20524	1.03
Br	0.01023	4.129	-0.63

**Table 1.** Force field parameters for potential model.

the nuclear-nuclear interactions than the LJ potential in short-range. The atsim.potentials package [19] is used to perform the spline.

$$\begin{aligned}
 V(r) &= \frac{1}{4\pi\epsilon_0} \frac{Z_1}{Z_2} \phi(r/a) + S(r) \\
 a &= \frac{0.46850}{Z_i^{0.23} + Z_j^{0.23}} \\
 \phi(x) &= 0.18175 \exp(-3.19980x) \\
 &\quad + 0.50986 \exp(-0.94229x) \\
 &\quad + 0.28022 \exp(-0.40290x) \\
 &\quad + 0.02817 \exp(-0.20162x)
 \end{aligned} \tag{4}$$

The potential curves variation with distance are illustrated in figure 2.

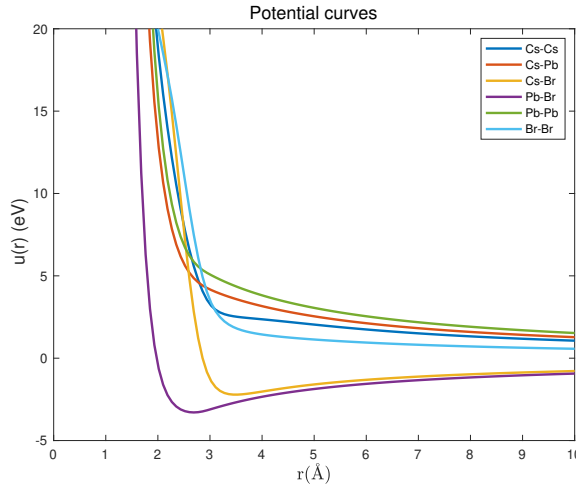


**Figure 2.** Potential curves for molecular dynamics simulations.

## Molecular dynamic simulation

### Search for threshold displacement energy

The threshold displacement energy is the minimum kinetic energy that an atom needs to be permanently displaced from its lattice site to a defect position. It is also known as "displacement threshold energy" or "displacement energy".

Large-scale Atomic/Molecular Massively Parallel Simulator (LAMMPS) [20] is used for molecular dynamics simulations in this study. Since the crystal structure of  $\text{CsPbBr}_3$  is highly symmetrical, it is not necessary to calculate every angle in space when calculating the threshold displacement energy. In this study, the spherical coordinate system was used, uniformly chosen phi as 0 to 90°, theta as 0 to 90°, and the angle step size was 5° for phi and theta. Totally, there are 361 directions.

To consider the balance between speed and accuracy of calculations, a simulation supercell ( $10 \times 10 \times 10$ ) containing 5000 atoms was applied. The NPT condition was applied to equilibrate the system until it reached the requirement of temperature. In this study, the system was equilibrated at specific temperatures, which are 100 K, 200 K, 300 K, and 400 K separately. The size of the system was minorly adjusted during the relaxation process. After the equilibrium, a Langevin thermostat was applied to the system's edge, and the microcanonical (NVE) ensemble was applied for cascade simulations. For each direction, a Cs, Pb or

Br atom around the central region of the system will be selected as a PKA. The Bisection method was used to obtain the threshold displacement energy for each type of atom. If the relationship between the velocity of PKA ( $v$ ) and the number of defects ( $N$ ) is written as  $f(v) = N$ , then the process will be illustrated as below:

1. Find two velocities, say  $v_1$  and  $v_2$ , such that  $v_1 < v_2$  and  $f(v_1) = 0$  and  $f(v_2) > 1$ .
2. Find the midpoint of  $v_1$  and  $v_2$ ; say  $v_3$ .
3.  $v_3$  is the final velocity of the given function if  $f(v_3) = 1$ ; else follow the next step.
4. Divide the interval  $[v_1, v_2]$  – If  $f(v_3) > 1$ , there exist a solution between  $v_1$  and  $v_3$  – else if  $f(v_3) = 0$ , there exist a solution between  $v_3$  and  $v_2$ .
5. Repeat above steps until  $f(v) = 1$ . The kinetic energy of an atom with velocity  $v_3$  is the threshold displacement energy in this direction.

The defect counting is the key to finding the threshold displacement energy from the process. The so-called Wigner-Seitz cell method implemented in OVITO [21] is used to count defects. The final frame from the equilibration simulation is used as the reference ‘defect-free’ configuration. The centre of a Wigner-Seitz cell is defined by each atom site of the reference frame. Any atom located within the Wigner-Seitz cell is said to occupy this site. By counting the number of atoms present in each Wigner-Seitz cell, vacancy, interstitial and antisite defects will be identified in subsequent frames. In threshold displacement energy simulations, the given displaced configuration frame is the final frame of the cascade simulation.

#### **radiation damage cascade**

To study the defects created by neutron radiation and high energy PKA to CsPbBr<sub>3</sub>, a simulation supercell 150×150×150 containing 16.875 million atoms is applied. The reason for the size of the supercell is to avoid the cascade reaching the cell boundary. The equilibration method is the same as the method used in threshold displacement energy simulations. In simulations, one Cs, Pb or Br atom was selected as high energy PKA. According to the results from Monte Carlo simulations, the average energy of PKA in CsPbBr<sub>3</sub> created by 14 MeV neutron flux is around 34 keV. Therefore, the energy PKA in cascade simulations is 34 keV. The microcanonical (NVE) ensemble was applied for cascade simulations, and a Langevin thermostat with a relaxation period of 10 ps was used around the supercell. The defect counting was carried out by the Python interface of OVITO using the Wigner-Seitz cell method.

#### **Monte Carlo simulation**

Monte Carlo simulations obtain the PKA energy spectrum and DPA. Geant4 toolkit was used to employ Monte Carlo simulations in this study. Figure 3 is the Monte Carlo simulation process in Geant4. The CsPbBr<sub>3</sub> construction in Geant4 is a cuboid with a 1 cm edge length and 300 μm height. The density is 4.42 g/cm<sup>3</sup>. The 14 MeV neutron source has a square shape with a 1 cm edge length. It was put on the 1 cm beyond the top surface of the CsPbBr<sub>3</sub>. The physics list used is FTFP\_BERT\_HP. The PKA spectrum was obtained, and according to the threshold displacement energy calculation results in this study, the values of DPA under different temperatures (100 K, 200 K, 300 K, 400 K) are calculated by the model illustrated in eq. (3) with considering the kinetic energy transfer [22].

$$N_d(T_d) = \begin{cases} 0, & T_d < E_d \\ 1, & E_d \leq T_d < \frac{2E_d}{0.8} \\ \frac{0.8T_d}{2E_d}, & \frac{2E_d}{0.8} \leq T_d < \infty \end{cases} \quad (5)$$

Where  $N_d$  is the predicted number of atom displacements and  $T_d$  is the damage energy (eV), which is the kinetic energy transferred to PKA from a neutron in this study.  $E_d$  is the threshold displacement energy (eV).

## **RESULTS AND DISCUSSIONS**

### **Threshold displacement energies**

The average threshold displacement energies for three atom sites are presented in table 2. Furthermore, the threshold displacement energies for 361 directions ( $\phi$  from 0° to 90°,  $\theta$  from 0° to 90°) under different

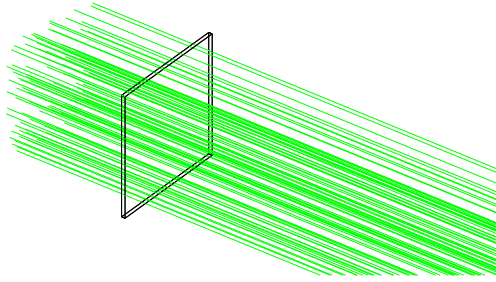


**Figure 3.** Schematic diagram of Geant4 simulation process.

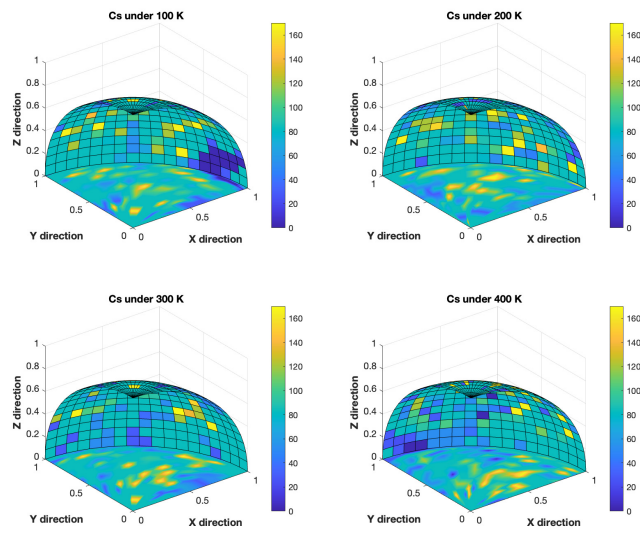


**Figure 4.** Spatial distribution of threshold displacement energy for Cs site.

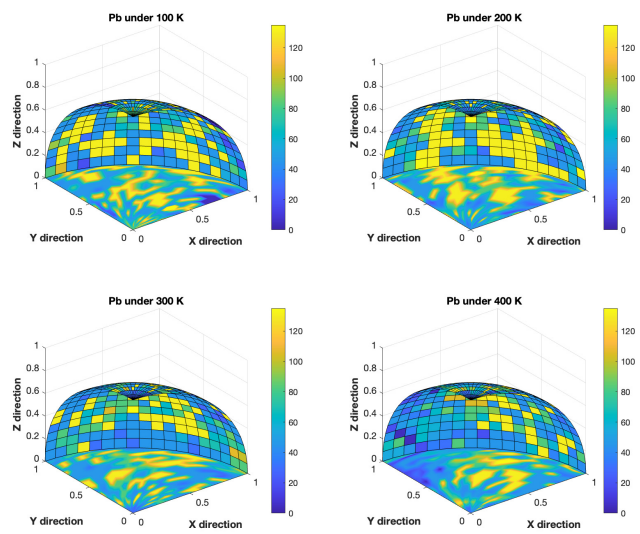


**Figure 5.** Spatial distribution of threshold displacement energy for Pb site

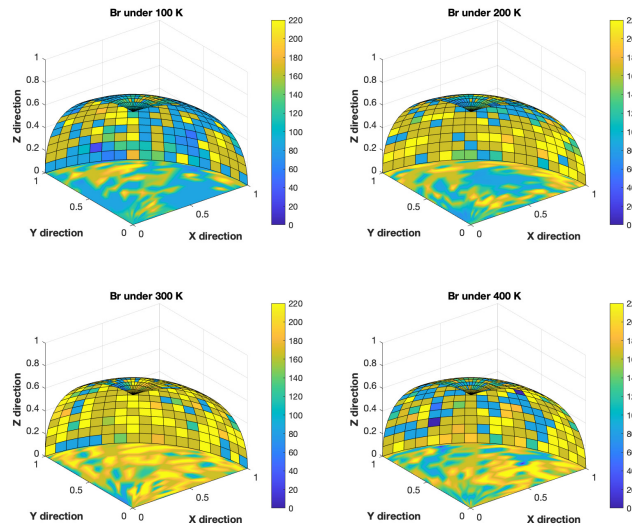


**Figure 6.** Spatial distribution of threshold displacement energy for Br site

TDE \ T	100 K	200 K	300 K	400 K
Site				
Cs	76.86	80.69	80.12	76.96
Pb	69.84	68.28	63.24	58.64
Br	70.19	81.25	97.03	90.47
Average	71.45	78.55	86.89	81.40

**Table 2.** Threshold displacement energies for each site and different temperature.

temperatures are illustrated in figs. 4 to 6. For Cs, Pb, and Br atom sites, the displacement energy ranges are 76.86 eV to 80.69 eV, 58.64 eV to 69.84 eV and 70.19 eV to 97.03 eV.

From table 2, for the Cs atom site and Br atom site, the average threshold displacement energy will increase with the increasing temperature until 300 K. The displacement energy will decrease when the temperature turns up constantly after 300 K. However, the case is not suitable for Pb atom site. This phenomenon is about the temperature dependence of the threshold displacement energy. When a neutron transfers kinetic energy to the PKA, the PKA moves and collides with surrounding atoms in a cascade, this process will form many Frenkel defect pairs. However, these Frenkel defect pairs are not permanent. There is the possibility that the atoms which kicked out of the site will be dragged back under the influence of potentials. Therefore, the threshold displacement energy will be higher than the formation energy of the Frenkel defect.

What's more, this process is more likely to occur at a high temperature, and this explains why the threshold displacement energy will increase firstly with the increased temperature. However, the threshold displacement energy will decrease if the temperature is higher than a specific value because the atom's thermal motion is strengthened. This means it will create a balance between the kick-off stage and the recombination stage with the effect of temperature.

In this study, from table 2, the average threshold displacement energy of Pb decreases Continuously with the increased temperature. An explanation for this could be that the Pb has the most significant mass in these three types of atoms. Therefore, its atomic motion has excellent inertia, which could easily create stable defects. What's more, as mentioned in the last paragraph, the increased temperature will enhance the thermal motion of Pb, which makes it difficult to stop a Pb PKA.

### Cascade process and PKA energies

fig. 7 is the PKA energy spectrum generated by 14 MeV neutrons. Among all generated PKAs, the proportions of Cs PKA, Pb PKA, and Br PKA are 25.3%, 24.7%, and 50%. Since the number of Br is the largest, its elastic scattering cross-section with neutrons is the largest. The average energy of Cs PKA, Pb Pka and Br PKA are 26 keV, 21 keV and 45 keV. As illustrated in fig. 7, the average energy of PKA is

around 34 keV.

Therefore, the discussion about radiation damage begins with the variation of defects created by 34 keV Cs, Pb and Br PKA over time under 300 K.

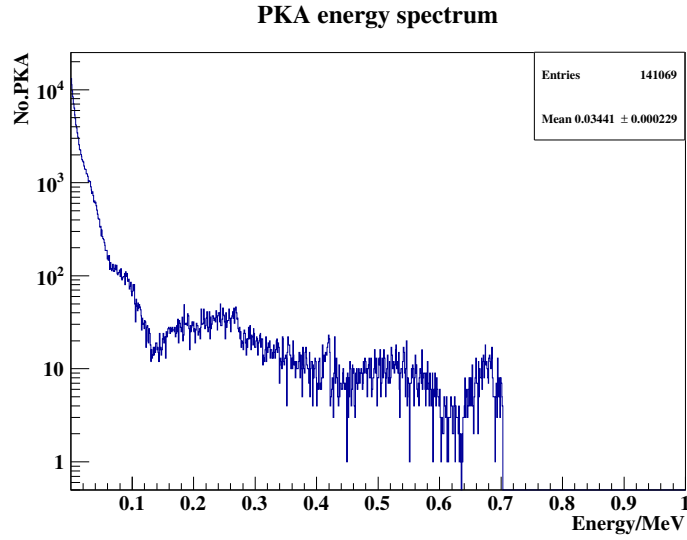


**Figure 7.** PKA energy spectrum of CsPbBr<sub>3</sub> with 14 MeV neutron irradiation

From fig. 8, Pb PKA generated the highest number of defects for the off-site peak and recombination process. This is due to the lowest threshold displacement energy of Pb, which was studied in the previous section. The highest number of defects generated by a 34 keV Pb PKA is 3587 at 3.0 *ps*. The highest number of defects generated by a 34 keV Cs PKA is 2972 at 3.5 *ps*. For Br PKA, compared to the defects produced by Cs PKA and Pb PKA, the highest number of defects, which is 2611, appears at 7.25 *ps*. This is because the threshold displacement energy of Br is the highest as PKA has lost much kinetic energy after leaving the lattice, and the Br atoms are also surrounded by Br atoms. It is difficult to generate many defects at first, but as the surrounding Pb SKA and Cs SKA take part in the cascade process, defects gradually increase.

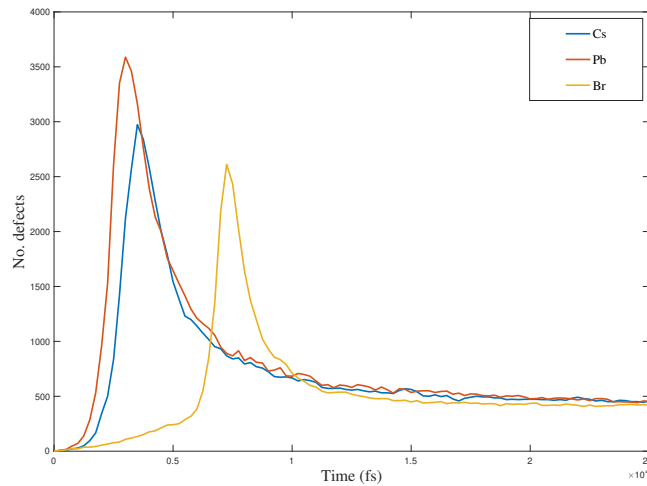


**Figure 8.** Time evolution of defects produced by 34 keV Cs, Pb or Br PKA.

Then, antisite atoms are also investigated. In a cascading collision, a site may be occupied by atoms of different types. For example, in CsPbBr<sub>3</sub>, a site of Pb occupied by Cs can be written as Cs on Pb antisite. Like the study on the total number of defects change over time, the numbers of different antisite atoms change over time were studied. Due to the symmetry crystal structure of CsPbBr<sub>3</sub>, there are six types of antisite atoms, which are: Pb on cs, br on cs, cs on pb, br on pb, cs on br and pb on br. As illustrated in fig. 9, except for Pb antisite on cs and cs antisite on Pb, the number of other antisite atoms will decrease to

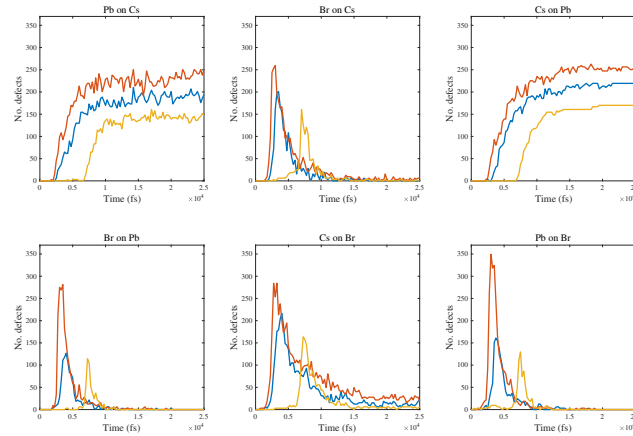


**Figure 9.** Time evolution of antisites produced by 34 keV Cs, Pb or Br PKA.

zero.

In contrast, the number of Pb on Cs and Cs on Pb will increase from zero to a specific value. It indicated that these two antisites are the two primary antisites after the cascade process. This provides a new direction to improve the high energy neutron radiation tolerance for CsPbBr<sub>3</sub>, reducing the Pb on Cs and Cs on Pb and their effects on the material.

With the obtained average threshold displacement energy of CsPbBr<sub>3</sub> and Monte Carlo simulations, the DPA caused by 14 MeV neutron flux was obtained, which is  $4.35 \times 10^{-22}$ . In this study, the unit of DPA is  $DPA \times cm^2 / incident\ particles$  [22].

## CONCLUSIONS

In summary, the effect of neutron radiation on CsPbBr<sub>3</sub> was investigated. The threshold displacement energies of three different atoms in 361 directions (phi from 0 to 90, theta from 0 to 90) were obtained. After that, the number of defects, the number of antisite atoms and the defect types caused by three different PKAs at 34 keV energy were investigated. Under the same energy, Pb PKA caused the highest peak and the most significant number of defects. The two most common antisite atoms are pb on cs and cs on pb, which are not directly related to the type of PKA. Using the obtained threshold displacement energy, the calculation of the PKA energy spectrum and the numerical value of DPA at different temperatures were carried out using the Monte Carlo simulation method. This research will help verify the ability of CsPbBr<sub>3</sub> to work in a neutron radiation environment. The resulting data can be further contributed to dynamic Monte Carlo simulations to simulate radiation damage on larger time scales.

## AUTHOR CONTRIBUTIONS

Z.Z., S.M. and M.A. conceived the presented idea; Z.Z. wrote the main manuscript; All authors have read and agreed to the published version of the manuscript.

## FUNDING

This work was supported School of Engineering, Lancaster University. For the purpose of open access, the author has applied a CC BY public copyright licence to any Author Accepted Manuscript version arising from this submission.

## CONFLICTS OF INTEREST

The authors declare no conflict of interest.



## REFERENCE

- [1] R. W. Conn, S. Sharafat, F. Najmabadi, R. W. Conn, S. Sharafat, F. Najmabadi, J. P. Holdren, D. Steiner, D. A. Ehst, W. J. Hogan, R. A. Krakowski, R. L. Miller, and K. R. Schultz. Economic, safety and environmental prospects of fusion reactors. *Nuclear Fusion*, 30(9):1919–1934, 1990.
- [2] H. Brysk. Fusion neutron energies and spectra. *Plasma Physics*, 15(7):611–617, 1973.
- [3] R L Gray, M J D Rushton, and S T Murphy. Molecular dynamics simulations of radiation damage in YBa<sub>2</sub>Cu<sub>3</sub>O<sub>7</sub>. *Superconductor Science and Technology*, 35(3):35010, feb 2022.
- [4] Constantinos C. Stoumpos, Christos D. Malliakas, John A. Peters, Zhifu Liu, Maria Sebastian, Jino Im, Thomas C. Chasapis, Arief C. Wibowo, Duck Young Chung, Arthur J. Freeman, Bruce W. Wessels, and Mercouri G. Kanatzidis. Crystal growth of the perovskite semiconductor CsPbBr<sub>3</sub>: A new material for high-energy radiation detection. *Crystal Growth and Design*, 13(7):2722–2727, 2013.
- [5] Jialong Duan, Yuanyuan Zhao, Benlin He, and Qunwei Tang. Simplified Perovskite Solar Cell with 4.1Inorganic CsPbBr<sub>3</sub> as Light Absorber. *Small*, 14(20):1–6, 2018.
- [6] Zheng Zhang and Bayram Saparov. Charge carrier mobility of halide perovskite single crystals for ionizing radiation detection. 030502(July), 2021.
- [7] Yuhai Zhang, Ruijia Sun, Xiangyu Ou, Kaifang Fu, Qiushui Chen, Yuchong Ding, Liang Jin Xu, Lingmei Liu, Yu Han, Anton V. Malko, Xiaogang Liu, Huanghao Yang, Osman M. Bakr, Hong Liu, and Omar F. Mohammed. Metal Halide Perovskite Nanosheet for X-ray High-Resolution Scintillation Imaging Screens. *ACS Nano*, 2019.
- [8] Lei Pan, Yuanxiang Feng, Praneeth Kandlakunta, Jinsong Huang, and Lei R. Cao. Performance of Perovskite CsPbBr<sub>3</sub> Single Crystal Detector for Gamma-Ray Detection. *IEEE Transactions on Nuclear Science*, 67(2):443–449, 2020.
- [9] Lidia El Bouanani, Sheila E. Keating, Carlos Avila-Avendano, Martin Gregorio Reyes-Banda, Maria Isabel Pintor-Monroy, Vidushi Singh, Bayron L. Murillo, Marissa Higgins, and Manuel A. Quevedo-Lopez. Solid-State Neutron Detection Based on Methylammonium Lead Bromide Perovskite Single Crystals. *ACS Applied Materials & Interfaces*, 13(24):28049–28056, 2021.
- [10] Sy Bing Choi, Beow Keat Yap, Yee Siew Choong, and Habibah Wahab. Molecular dynamics simulations in drug discovery. *Encyclopedia of Bioinformatics and Computational Biology: ABC of Bioinformatics*, 1-3:652–665, 2018.
- [11] Huan He, Chaohui He, Jiahui Zhang, Wenlong Liao, Hang Zang, Yonghong Li, and Wenbo Liu. Primary damage of 10 keV Ga PKA in bulk GaN material under different temperatures. *Nuclear Engineering and Technology*, 52(7):1537–1544, 2020.
- [12] J. T. Buchan, M. Robinson, H. J. Christie, D. L. Roach, D. K. Ross, and N. A. Marks. Molecular dynamics simulation of radiation damage cascades in diamond. *Journal of Applied Physics*, 117(24), 2015.
- [13] Zhong Rui, Baoqin Fu, Jiechao Cui, and Qing Hou. Molecular dynamics simulation of self-radiation damages in zirconium and defects identification research. *Journal of Sichuan University*, 57(1), 2020.
- [14] J. Allison, K. Amako, J. Apostolakis, P. Arce, M. Asai, T. Aso, E. Bagli, A. Bagulya, S. Banerjee, G. Barrand, B. R. Beck, A. G. Bogdanov, D. Brandt, J. M.C. Brown, H. Burkhardt, Ph Canal, D. Cano-Ott, S. Chauvie, K. Cho, G. A.P. Cirrone, G. Cooperman, M. A. Cortés-Giraldo, G. Cosmo, G. Cuttone, G. Depaola, L. Desorgher, X. Dong, A. Dotti, V. D. Elvira, G. Folger, Z. Francis, A. Galoyan, L. Garnier, M. Gayer, K. L. Genser, V. M. Grichine, S. Guatelli, P. Guèye, P. Gumplinger, A. S. Howard, I. Hřivnáčová, S. Hwang, S. Incerti, A. Ivanchenko, V. N. Ivanchenko, F. W. Jones, S. Y. Jun, P. Kaitaniemi, N. Karakatsanis, M. Karamitrosi, M. Kelsey, A. Kimura, T. Koi, H. Kurashige, A. Lechner, S. B. Lee, F. Longo, M. Maire, D. Mancusi, A. Mantero, E. Mendoza, B. Morgan, K. Murakami, T. Nikitina, L. Pandola, P. Paprocki, J. Perl, I. Petrović, M. G. Pia, W. Pokorski, J. M. Quesada, M. Raine, M. A. Reis, A. Ribon, A. Ristić Fira, F. Romano, G. Russo, G. Santin, T. Sasaki, D. Sawkey, J. I. Shin, I. I. Strakovsky, A. Taborda, S. Tanaka, B. Tomé, T. Toshito, H. N. Tran, P. R. Truscott, L. Urban, V. Uzhinsky, J. M. Verbeke, M. Verderi, B. L. Wendt, H. Wenzel, D. H. Wright, D. M. Wright, T. Yamashita, J. Yarba, and H. Yoshida. Recent developments in GEANT4. *Nuclear Instruments and Methods in Physics Research, Section A: Accelerators, Spectrometers, Detectors and Associated Equipment*, 835:186–225, 2016.
- [15] S. Agostinelli, J. Allison, K. Amako, J. Apostolakis, H. Araujo, P. Arce, M. Asai, D. Axen, S. Banerjee, G. Barrand, F. Behner, L. Bellagamba, J. Boudreau, L. Broglia, A. Brunengo, H. Burkhardt, S. Chauvie, J. Chuma, R. Chytrcek, G. Cooperman, G. Cosmo, P. Degtyarenko, A. Dell’Acqua, G. Depaola, D. Dietrich, R. Enami, A. Feliciello, C. Ferguson, H. Fesefeldt, G. Folger, F. Foppiano, A. Forti, S. Garelli, S. Giani, R. Giannitrapani, D. Gibin, J. J. Gomez Cadenas, I. Gonzalez, G. Gracia Abril, G. Greeniaus, W. Greiner, V. Grichine, A. Grossheim, S. Guatelli, P. Gumplinger, R. Hamatsu, K. Hashimoto, H. Ha-sui, A. Heikkinen, A. Howard, V. Ivanchenko, A. Johnson, F. W. Jones, J. Kallenbach, N. Kanaya,

- M. Kawabata, Y. Kawabata, M. Kawaguti, S. Kelner, P. Kent, A. Kimura, T. Kodama, R. Kokoulin, M. Kossov, H. Kurashige, E. Lamanna, T. Lampen, V. Lara, V. Lefebure, F. Lei, M. Liendl, W. Lockman, F. Longo, S. Magni, M. Maire, E. Medernach, K. Minamimoto, P. Mora de Freitas, Y. Morita, K. Murakami, M. Nagamatu, R. Nartallo, P. Nieminen, T. Nishimura, K. Ohtsubo, M. Okamura, S. O’Neale, Y. Oohata, K. Paech, J. Perl, A. Pfeiffer, M. G. Pia, F. Ranjard, A. Rybin, S. Sadilov, E. di Salvo, G. Santin, T. Sasaki, N. Savvas, Y. Sawada, S. Scherer, S. Sei, V. Sirotenko, D. Smith, N. Starkov, H. Stoecker, J. Sulkimo, M. Takahata, S. Tanaka, E. Tcherniaev, E. Safai Tehrani, M. Tropeano, P. Truscott, H. Uno, L. Urban, P. Urban, M. Verderi, A. Walkden, W. Wander, H. Weber, J. P. Wellisch, T. Wenaus, D. C. Williams, D. Wright, T. Yamada, H. Yoshida, and D. Zschiesche. GEANT4 - A simulation toolkit. *Nuclear Instruments and Methods in Physics Research, Section A: Accelerators, Spectrometers, Detectors and Associated Equipment*, 506(3):250–303, 2003.
- [16] Kristin Persson. Materials Data on CsPbBr<sub>3</sub> (SG:221) by Materials Project. (July), 2014.
  - [17] Connor G. Bischak, Minliang Lai, Zhaochuan Fan, Dylan Lu, Philippe David, Dengpan Dong, Hong Chen, Ahmed S. Etman, Teng Lei, Junliang Sun, Michael Grünwald, David T. Limmer, Peidong Yang, and Naomi S. Ginsberg. Liquid-like Interfaces Mediate Structural Phase Transitions in Lead Halide Perovskites. *Matter*, 3(2):534–545, 2020.
  - [18] James F Ziegler, Matthias D Ziegler, and Jochen P Biersack. Srim—the stopping and range of ions in matter (2010). *Nuclear Instruments and Methods in Physics Research Section B: Beam Interactions with Materials and Atoms*, 268(11-12):1818–1823, 2010.
  - [19] M Rushton. atsim. potentials—potential model tabulation for atomic scale simulation. 2018.
  - [20] Steve Plimpton. Fast parallel algorithms for short-range molecular dynamics. *Journal of computational physics*, 117(1):1–19, 1995.
  - [21] Alexander Stukowski. Visualization and analysis of atomistic simulation data with ovito—the open visualization tool. *Modelling and simulation in materials science and engineering*, 18(1):015012, 2009.
  - [22] Zhongming Zhang and Michael D. Aspinall. Comparison of neutron detection performance of four thin-film semiconductor neutron detectors based on geant4. *Sensors*, 21(23), 2021.